

## THE RADIAL DISTRIBUTION OF GALAXIES IN $\Lambda$ CDM CLUSTERS

DAISUKE NAGAI<sup>1</sup> AND ANDREY V. KRAVTSOV<sup>1</sup>

Department of Astronomy and Astrophysics, Kavli Institute for Cosmological Physics,  
5640 South Ellis Ave., The University of Chicago, Chicago, IL 60637  
The Astrophysical Journal, submitted

### ABSTRACT

We study the radial distribution of subhalos and galaxies using high-resolution cosmological simulations of galaxy clusters formed in the concordance  $\Lambda$ CDM cosmology. In agreement with previous studies, we find that the radial distribution of subhalos is significantly less concentrated than that of the dark matter, when subhalos are selected using their present-day gravitationally bound mass. We show that the difference in the radial distribution is not a numerical artifact and is due to tidal stripping. The subhalos in the cluster core lose more than 70% of their initial mass since accretion, while the average tidal mass loss for halos near the virial radius is  $\approx 30\%$ . This introduces a radial bias in the spatial distribution of subhalos when the subhalos are selected using their tidally truncated mass. We demonstrate that the radial bias disappears almost entirely if subhalos are selected using their mass or circular velocity at the accretion epoch. The comparisons of the results of dissipationless simulations to the observed distribution of galaxies in clusters are therefore sensitive to the selection criteria used to select subhalo samples. Using the simulations that include cooling and starformation, we show that the radial distribution of subhalos is in reasonable agreement with the observed radial distribution of galaxies in clusters over the entire radial range probed by the simulations,  $0.1 < R/R_{200} < 2.0$ , if subhalos are selected using the stellar mass of galaxies they harbor. The radial bias is minimized in this case because the stars are located in the centers of dark matter subhalos and are tightly bound. The stellar mass of an object is therefore approximately conserved as the dark matter is stripped from the outer regions. Nevertheless, the concentration of the radial distribution of galaxies is systematically lower than that of the dark matter. Finally, we find that the baryon dissipation does enhance the survival of subhalos, especially in the cluster cores. However, the effect is relatively weak because the baryon dissipation affects the density distribution only at small radii.

*Subject headings:* cosmology: theory–galaxies: formation– methods: numerical

### 1. INTRODUCTION

Understanding the spatial distribution of galaxies and matter is one of the main goals of observational and theoretical cosmology. At large scales, the galaxy and matter distributions on average are thought to be simply related by a constant scale-independent bias, with the constant depending on the galaxy mass (e.g., Mo & White 1996; Scherrer & Weinberg 1998). Clustering of galaxies at small scales ( $r \lesssim 3h^{-1}$  Mpc), on the other hand, is thought to be determined by the abundance and radial distribution of galaxies within dark matter halos (e.g., see Cooray & Sheth 2002, for a recent review).

While the abundance of galaxies in halos of different mass have recently been extensively quantified in cosmological simulations (e.g., Seljak 2000; Guzik & Seljak 2001; White et al. 2001; Berlind et al. 2003; Kravtsov et al. 2004a), their radial distribution is less well understood. Theoretical analyses often simply assume that galaxies trace the radial profile of dark matter. However, it is easy to imagine that dynamical friction, tidal disruption, and morphological transformation could modify the distribution of galaxies with respect to matter. In addition, the radial distribution of galaxies should clearly be sensitive to how galaxies are selected. For example, the distribution of early type red galaxies in clusters is more centrally concentrated than that of late type blue galaxies (e.g., Goto et al. 2004). New cluster samples based on large galaxy surveys (Carlberg et al. 1997; van der Marel et al. 2000; Lin et al.

2004; Miller et al. 2004) should shed light on these issues, but the interpretation of observational results will require comparisons with theoretical expectations.

Properties of galaxy-size dark matter halos in groups and clusters (or *the subhalos*) have been the subject of many recent studies, which used a new generation of high-resolution dissipationless simulations not affected by the “overmerging” problem (Ghigna et al. 1998; Tormen et al. 1998; Klypin et al. 1999; Colín et al. 1999; Okamoto & Habe 1999; Colín et al. 2000; Ghigna et al. 2000; Springel et al. 2001; Taffoni et al. 2003; De Lucia et al. 2004; Tormen et al. 2004; Kravtsov et al. 2004b; Diemand et al. 2004; Gao et al. 2004b; Reed et al. 2004). One of the main results is that the radial distribution of subhalos is less concentrated than that of dark matter (Ghigna et al. 1998; Colín et al. 1999; Ghigna et al. 2000; Springel et al. 2001; De Lucia et al. 2004; Gao et al. 2004a). The subhalos also appear to have a significantly more extended and shallower radial distribution compared to the observed distribution of galaxies in clusters, a point recently emphasized by Diemand et al. (2004) and Gao et al. (2004a).

Although questions were raised about remaining overmerging in the inner regions of halos (Taylor et al. 2003), Diemand et al. (2004) used convergence tests to show that the subhalo distribution is not affected by resolution but is due to real physical merging of subhalos in dissipationless simulations (see also § 4 below). They also argued that the physical overmerging in dissipationless simulations results in a factor of two underestimate of the number of galactic subhalos in cluster-size systems.

<sup>1</sup> daisuke, andrey@oddjob.uchicago.edu

One of the obvious omissions in dark matter only simulations is the lack of dissipation and starformation. After all, the observed samples of galaxies are most often selected using their luminosity or an observational proxy for stellar mass, not a total gravitationally bound mass. In addition, when baryons cool and condense in the cores of dark matter halos, they increase the inner density of their host, which can make it more resistant to tidal disruption (White & Rees 1978). It is therefore important to test whether inclusion of cooling and starformation, the processes critical for realistic modeling of galaxy formation, results in significantly different galaxy populations in clusters.

Although a number of studies during the last decade used gasdynamics cosmological simulations with cooling to study galaxy clustering on small scales (e.g., Katz et al. 1992; Pearce et al. 1999; Blanton et al. 2000; Yoshikawa et al. 2001; Weinberg et al. 2004), only a few analyses directly addressed the radial distribution of galaxies in halos. Frenk et al. (1996) used simulations with cooling and starformation to study distribution and dynamics of galaxies in clusters. They found that stellar systems formed in the simulations were more centrally concentrated than dark matter. This, however, was the case only in the runs with starformation. When gas was allowed to cool without forming stars, the simulations appeared to suffer from the “overmerging” problem. More recently, Berlind et al. (2003) analyzed the radial distribution of galaxies, identified as dense baryonic clumps, in halos of different mass in SPH simulations. These authors found that galaxies selected to have baryonic masses above a certain threshold have a somewhat more extended distribution compared to the dark matter.

A number of studies used a hybrid approach of combining high-resolution  $N$ -body simulations with semi-analytic models of galaxy formation to study galaxy populations in clusters and groups (Springel et al. 2001; Okamoto & Nagashima 2001; Kravtsov et al. 2004b; Gao et al. 2004a). All of these models imply that radial distribution of halos is more extended than that of the luminous galaxies. By necessity, semi-analytic studies make certain assumptions about dynamical evolution of the stellar component, not included directly in simulations. For example, Springel et al. (2001) and Gao et al. (2004a) find that for a large fraction of objects in the cluster core the stellar systems may survive as distinct galaxies, even after their DM halos are disrupted. Kravtsov et al. (2004b) used the tidal force measured in simulations to estimate the amount of tidal heating and mass loss of galaxies semi-analytically.

It is clearly important to address the radial distribution of subhalos and galaxies in self-consistent high-resolution cosmological simulations of cluster formation. In this paper, we present such a study. We compare results of cluster simulations with gasdynamics, cooling, and starformation to the dissipationless simulations started from the same initial conditions. We test the convergence of our results by comparing results of two simulations of the same cluster with an order of magnitude different resolution.

The paper is organized as follows. In the following two sections, we describe the numerical simulations and halo finding algorithm used in our analysis. In § 4 we present the convergence tests. We present the results of dissipa-

tionless simulations in § 5 and gasdynamics simulations in § 6. We summarize our results and conclusions in § 7.

## 2. SIMULATIONS

In this study, we analyze high-resolution cosmological simulations of eight group and cluster-size systems in the “concordance” flat  $\Lambda$ CDM model:  $\Omega_m = 1 - \Omega_\Lambda = 0.3$ ,  $\Omega_b = 0.043$ ,  $h = 0.7$  and  $\sigma_8 = 0.9$ , where the Hubble constant is defined as  $100h \text{ km s}^{-1} \text{ Mpc}^{-1}$ , and  $\sigma_8$  is the power spectrum normalization on  $8h^{-1} \text{ Mpc}$  scale. The virial masses of cluster systems we consider range from  $\approx 7 \times 10^{13} h^{-1} M_\odot$  to  $3 \times 10^{14} h^{-1} M_\odot$ . The simulations were done with the Adaptive Refinement Tree (ART)  $N$ -body+gasdynamics code (Kravtsov 1999; Kravtsov, Klypin, & Hoffman 2002), an Eulerian code, which uses the adaptive refinement in space and time, and (non-adaptive) refinement in mass (Klypin et al. 2001) to reach the high dynamic range required to resolve cores of halos formed in self-consistent cosmological simulations.

For each cluster, we analyze two sets of simulations started from the same initial conditions but with different physical processes included. The first set of simulations followed dynamics of dark matter only. To study effects of resolution, one of the clusters was re-simulated with eight times more particles and with higher spatial resolution (Tasitsiomi et al. 2004). We will be denoting lower and higher resolution simulations of this cluster as LR and HR runs. Both LR and HR runs used a  $256^3$  uniform root grid covering the computational box of  $80h^{-1} \text{ Mpc}$ , but different numbers of particles and refinements. The LR run has an effective mass resolution of  $m_p^{\text{LR}} = 3.16 \times 10^8 h^{-1} M_\odot$ , corresponding to  $512^3$  particles in the box, and reached 8 levels of refinement, corresponding to the size of the highest refinement level cell of  $1.2h^{-1} \text{ kpc}$ . The HR run has eight times more particles ( $m_p^{\text{HR}} = 3.95 \times 10^7 h^{-1} M_\odot$ ). In this simulation, the smallest cell size reached was  $0.6h^{-1} \text{ comoving kpc}$ .

The gasdynamics simulations started from the same initial conditions as the  $N$ -body runs used a  $128^3$  uniform grid and 8 levels of mesh refinement, which corresponds to the dynamic range of  $128 \times 2^8 = 32768$  and peak resolution of  $80/32,768 \approx 2.44h^{-1} \text{ kpc}$ . Only the region of  $\sim 10h^{-1} \text{ Mpc}$  around the cluster was adaptively refined, the rest of the volume was followed on the uniform  $128^3$  grid. The dark matter particle mass in the region around the cluster was  $2.7 \times 10^8 h^{-1} M_\odot$ , while other regions were simulated with lower mass resolution. Note that although the mass resolution of the gasdynamics and the LR  $N$ -body run is similar, the spatial resolution in the latter is higher. In addition, more aggressive refinement criteria were used in the  $N$ -body runs compared to the gasdynamics simulations. Some differences in the completeness of subhalo samples are therefore expected.

The gasdynamics simulations included dynamics of gas and collisionless DM and several physical processes critical to various aspects of galaxy formation: star formation, metal enrichment and thermal feedback due to the supernovae type II and type Ia (SNII/Ia), self-consistent advection of metals, metallicity- and density-dependent cooling and UV heating due to cosmological ionizing background using cooling and heating rates tabulated for the temperature range  $10^2 < T < 10^9 \text{ K}$  and a grid of densities,

metallicities, and UV intensities using the Cloudy code (ver. 96b4, Ferland et al. 1998). The cooling and heating rates take into account Compton heating/cooling of plasma, UV heating, atomic and molecular cooling. Star formation in the cluster simulations is implemented using the observationally-motivated recipe (e.g., Kennicutt 1998):  $\dot{\rho}_* = \rho_{\text{gas}}^{1.5}/t_*$ , with  $t_* = 4 \times 10^9$  yrs. Stars are allowed to form in regions with temperature  $T < 2 \times 10^4$ K and gas density  $n > 0.1 \text{ cm}^{-3}$ . A more detailed description of these simulations will be presented elsewhere.

### 3. HALO IDENTIFICATION

A variant of the Bound Density Maxima halo finding algorithm (Klypin et al. 1999) is used to identify halos and the subhalos within them. The details of the algorithm and parameters used in the halo finder can be found in Kravtsov et al. (2004a). The main steps of the algorithm are identification of local density peaks (potential halo centers) and analysis of the density distribution and velocities of the surrounding particles to test whether a given peak corresponds to a gravitationally bound clump. More specifically, we construct density, circular velocity, and velocity dispersion profiles around each center and iteratively remove unbound particles using the procedure outlined in Klypin et al. (1999). We then construct final profiles using only bound particles and use these profiles to calculate properties of halos, such as the circular velocity profile  $V_{\text{circ}}(r) = \sqrt{GM(<r)/r}$  and compute the maximum circular velocity  $V_{\text{max}}$ .

If the center of a halo does not lie within a larger system, we consider the halo to be an isolated or *host* halo. In this case we use the virial radius,  $r_{\text{vir}}$ , defined as the radius enclosing an overdensity of 180 with respect to the mean density of the Universe<sup>2</sup>. For halos located within the virial radius of a larger host halo (*the subhalos*), we define the outer boundary at the truncation radius,  $r_t$ , at which the logarithmic slope of the density profile constructed from the bound particles becomes larger than  $-0.5$  as we do not expect the density profile of the CDM halos to be flatter than this slope. Throughout this paper, we will denote the minimum of the virial mass and mass within  $r_t$ , simply as  $M$ . In the gasdynamics simulations, the total mass of an object includes the mass of dark matter, gas, and stars. For each system we also estimate the stellar mass,  $M_*$ , within the truncation radius.

### 4. CONVERGENCE TESTS

Before we proceed with our analysis, it is important to test the effects of resolution and determine the smallest mass of objects that are resolved and identified reliably in our simulations. Figure 1 shows comparison of the cumulative mass functions of subhalos in the two  $N$ -body and gasdynamics simulations of the same cluster. We present separate comparisons for the objects within the virial radius and within the inner half of the virial radius to show any dependence on radius.

Note that small differences both between gasdynamics and  $N$ -body simulations and between low- and high-

<sup>2</sup> We will use this definition of the virial radius throughout the paper. In § 6.3, to compare the radial distributions of galaxies in simulations and observations we will use  $R_{200}$ , defined as the radius enclosing the overdensity of 200 with respect to the *critical* density of the Universe.

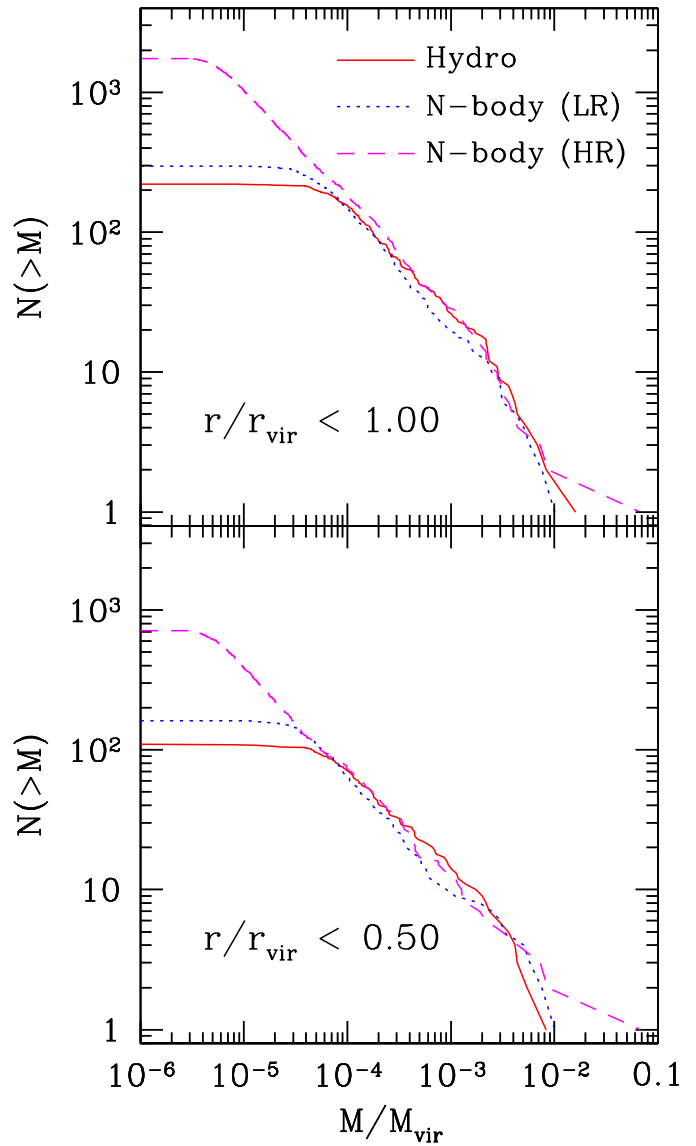


FIG. 1.— Cumulative mass function of subhalos enclosed within  $r_{\text{vir}}$  (top) and  $0.5r_{\text{vir}}$  (bottom) of the galaxy cluster with  $M_{\text{vir}} = 2.4 \times 10^{14} h^{-1} M_{\odot}$ . Three lines indicate gasdynamics run with cooling and starformation (solid), LR (dotted), and HR (dashed)  $N$ -body runs. The mass functions of all three runs converge for  $N_p \gtrsim 80$ , which corresponds to  $M/M_{\text{vir}} > 10^{-4}$  for hydro and LR runs and  $M/M_{\text{vir}} \gtrsim 10^{-5}$  for the HR  $N$ -body run.

resolution dissipationless simulations are expected even at masses where convergence is reached. The former can arise due to different time integration in the  $N$ -body and hydro codes (see, Frenk et al. 1999), while the latter can be due to the fact that the HR run includes small-scale modes absent in the LR run. With this in mind, comparisons of the mass functions in the LR  $N$ -body run and gasdynamics run agree well with the results of the HR  $N$ -body run for  $N_p \gtrsim 80$  or  $M/M_{\text{vir}} > 1 \times 10^{-4}$ . Similar comparison of the velocity functions of subhalos in the LR  $N$ -body run agree well with the results of the HR  $N$ -body run for  $V_m/V_{\text{vir}} > 0.1$  or  $V_m > 100$  km/s for the cluster halo with  $V_{\text{vir}} = 1065$  km/s. We will therefore only consider objects with masses and maximum circular velocities above these

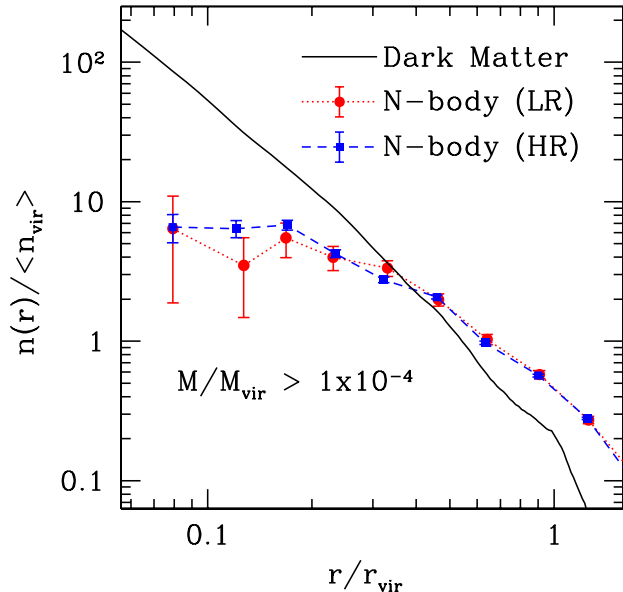


FIG. 2.— Convergence test for the radial distribution of subhalos in the same cluster as in Figure 1. Number density profiles of subhalos normalized to the number density within the virial radius,  $n(r)/\langle n_{\text{vir}} \rangle$ , in the HR (dotted) and LR (dashed)  $N$ -body runs for subhalos with masses  $M/M_{\text{vir}} > 10^{-4}$ . The solid line shows the dark matter profile normalized to the virial overdensity. The figure shows that the convergence for the radial distribution of subhalos is reached, as the profiles are similar in LR and HR runs.

limits in our analyses. We find no radial dependence of the slope of the cumulative mass and velocity functions. These results are in agreement with the convergence studies of Diemand et al. (2004) and Gao et al. (2004b).

Figure 2 shows the radial number density profiles of subhalos with total masses  $> 10^{-4} M_{\text{vir}}$  in the LR and HR  $N$ -body runs. The profiles are obtained by averaging over five (forty) outputs between  $z = 0.25$  and  $z = 0$  for the LR (HR)  $N$ -body runs, respectively<sup>3</sup>. For comparison of dark matter and subhalos, we normalize the profiles to the mean density within the virial radius,  $\langle n_{\text{vir}} \rangle$ . The figure shows that the profiles agree at all probed radii. The convergence is real and the subhalo profiles match without normalization (in other words, for the same mass threshold  $\langle n_{\text{vir}} \rangle$  is the same). This shows that both the normalization and shape of the radial profile of subhalos have converged for the current resolution of the LR  $N$ -body run. We therefore conclude that the difference between matter and subhalo distributions is real and is not due to numerical overmerging, in agreement with Diemand et al. (2004) and Gao et al. (2004b). This is inconsistent with the semi-analytic models of Taylor et al. (2003), which predict a considerably more radially concentrated distribution of subhalos than is observed in simulations.

## 5. DISSIPATIONLESS SIMULATIONS

In this section, we present the analyses of the dissipationless simulations to study the radial distribution of subhalos and how it depends on the selection criteria used to define subhalo sample. Figure 3 shows the radial number

<sup>3</sup> The difference in the number of epochs used in averaging is due to fewer outputs saved in the LR run.

density profiles normalized to the mean number density of subhalos within the virial radius in the HR  $N$ -body run. The four panels show the radial distribution of subhalos with different selection criteria. The top panels show the profile where the subhalos are selected using the present-day values of the subhalo mass,  $M^0$ , and the maximum circular velocity,  $V_{\text{m}}^0$ . The bottom panels show the profiles where the values at the time of accretion onto the cluster are used. These values are obtained from the evolutionary tracks of each subhalo constructed as described by Kravtsov et al. (2004b). We define the accretion epoch as the time when a halo’s distance to the most massive cluster progenitor first becomes smaller than 1.5 of its virial radius (at this epoch).

The profiles are constructed by stacking forty outputs between  $z = 0.25$  and  $z = 0$  to increase the statistics and reduce fluctuations. Note that this cluster does not evolve significantly between  $z = 0.25$  and  $z = 0$ . We also checked that the results are not biased by the stacking procedure. Throughout the paper, the error bars indicate  $1\sigma$  Poisson error defined by the number of objects in each bin. Here and throughout, we normalize all profiles to the mean density within the virial radius because this allows unambiguous comparison of radial distributions of dark matter and of halos of different masses. We do not include the central galaxy in the first bin of the profiles.

We show each selection using three values of threshold mass or circular velocity. The values of the circular velocity thresholds are chosen to match the corresponding mass thresholds approximately. The shape of the profiles does not depend on the subhalo mass and is significantly shallower than the dark matter distribution for all mass thresholds. This is consistent with the results of Diemand et al. (2004).

The more extended distribution of subhalos compared to DM in this case is simply due to the fact that the subhalos in the inner regions have on average suffered larger tidal mass loss than the halos near the virial radius. Figure 4 shows the fractional mass loss and the change in  $V_{\text{max}}^5$  experienced by each subhalo since the epoch when it reached the maximum mass,  $M_{\text{max}}$ , in its evolution. The scatter for individual objects is large and non-Gaussian and is due to the wide distribution of accretion times and orbital parameters of subhalos. Nevertheless, there is a clear average trend of increasing mass loss at smaller radii. For instance, the halos within  $0.3r_{\text{vir}}$  on average have lost more than 70% of their mass since accretion. At  $r > 0.5r_{\text{vir}}$  the halos on average lose only  $\lesssim 40\%$  of their mass. Note also that the tidal mass loss is also accompanied by a slow decrease in  $V_{\text{max}}$  (Kravtsov et al. 2004b, see also Tormen et al. 2004). Mass-based selection thus biases the subhalo sample to large radii where the tidal stripping have depleted the number of objects in a given mass range to a lesser degree.

Figure 3 shows that the bias introduced by selecting subhalo samples using circular velocity thresholds,  $V_{\text{m}}^0$ , is smaller than in the selection based on mass. The bias is expected in this case because circular velocity evolves when a halo experiences tidal loss as  $V_{\text{m}} \propto M^{0.2-0.25}$  (Kravtsov et al. 2004b). The average relation between circular velocity and mass for isolated halos is  $V_{\text{m}} \propto M^{0.3}$  (e.g., Avila-Reese et al. 1999; Bullock et al. 2001). The mass

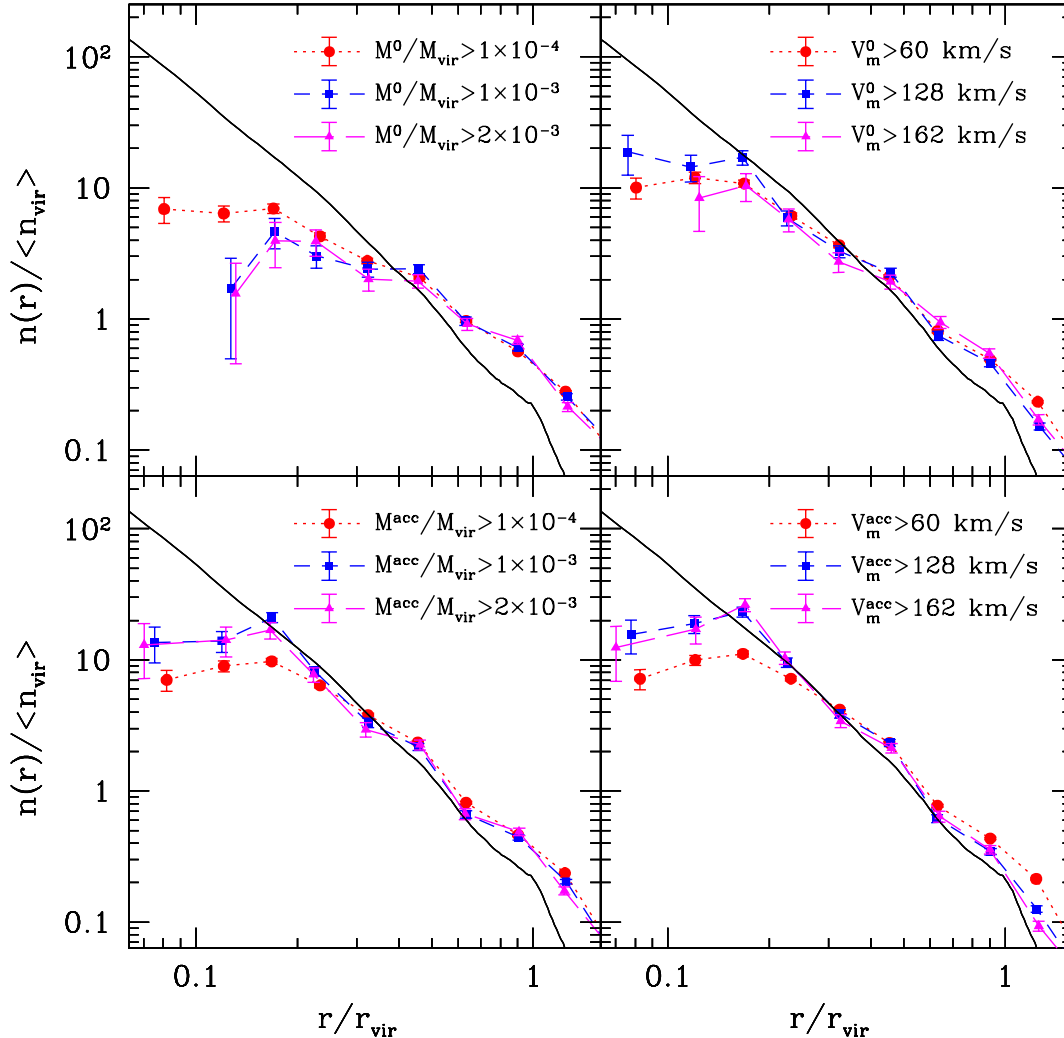


FIG. 3.— Radial distribution of subhalos for samples with different selection criteria. *Top panels:* the subhalos are selected using the present-day values of the subhalo total mass,  $M^0$ , (left) and the maximum circular velocity,  $V_m^0$  (right). *Bottom panels:* the subhalos are selected using the subhalo mass,  $M^{\text{acc}}$ , (left) and the maximum circular velocity,  $V_m^{\text{acc}}$  (right) at the time of accretion. In each panel the subhalos in the three samples were selected using either the minimum mass thresholds of  $M/M_{\text{vir}} > 10^{-4}$  (dotted),  $> 10^{-3}$  (dashed) and  $> 2 \times 10^{-3}$  (long-dashed) or corresponding values of the circular velocity:  $V_m > 60 \text{ km s}^{-1}$  (dotted),  $> 128 \text{ km s}^{-1}$  (dashed) and  $> 162 \text{ km s}^{-1}$  (long-dashed). The profiles are constructed by stacking 40 outputs of the HR  $N$ -body run between  $z = 0.25$  and  $z = 0$ . The error bars are the  $1\sigma$  Poisson errors, and the central galaxy is not included in the first bin of the profiles.

evolution would thus tend to shift the halos off the relation. Indeed we find that the normalization of the  $M - V_m$  relation changes for the smaller cluster-centric distances, although the slope of the relation is approximately constant. The slower evolution of the maximum circular velocity compared to mass means that when it is used to select subhalos the radial bias is smaller.

If the radial bias is due solely to the varying amount of mass loss at different radii, we can expect that it should be considerably smaller if we select subhalos using their mass or circular velocity at the time of accretion (i.e., not modified by the tidal stripping yet). The bottom panels of Figure 3 show the radial distribution of subhalos for such selections. It is clear that the subhalo radial profiles in this case are rather similar to the dark matter profile at  $r \gtrsim 0.2r_{\text{vir}}$ . The mass measured at the accretion, thus, provides a “label” for each object, which is not affected by

the subsequent tidal mass loss and evolution. Note that we can still expect a certain bias because a larger fraction of subhalos is fully disrupted by tides at small radii. We cannot compensate for the absence of the disrupted subhalos with the change of selection criteria for halos which survived to  $z = 0$ . We checked that the results are insensitive to the definition of time of accretion, as long as subhalos are selected based on their mass and  $V_m$  well before entering into the cluster virial region.

Our results therefore indicate that the bias in the radial distribution of subhalos with respect to dark matter arises simply due to the radial dependence of the effects of tidal stripping. It is minimized if we use a property of halos unaffected by the evolution. In dissipationless simulations such properties can only be computed at the actual time of accretion if the evolution of a halo is traced in time. Unfortunately, the halo properties at the time of accretion

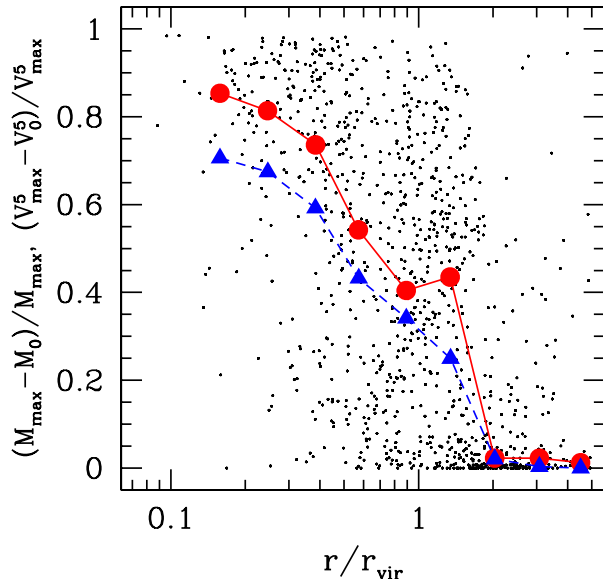


FIG. 4.— The fractional mass loss and the change in  $V_{\max}^5$  between the epochs when each subhalo has reached the maximum mass,  $M_{\max}$ , and  $z = 0$  as a function of the distance to the cluster center. The *dots* show the mass loss experienced by individual subhalos, while the *solid circles* show the median values in logarithmic radial bins. The *triangles* shows the same for the change in the fifth power of  $V_{\max}$ . Halos at smaller radii have on average experienced considerably more stripping than subhalos at larger radii. The tidal mass loss is also accompanied by the decrease in  $V_{\max}$ .

are not observable in reality. In the next section, we show that the stellar mass is an observable with similar properties. The stellar mass of an object should change little until it is almost fully destroyed by tides because stars are located in the centers of halos and are tightly bound. We can expect, therefore, that stellar mass should correlate well with the mass and circular velocity at the time of accretion and that the distribution of galaxies selected using stellar mass (or luminosity) should be similar to that of dark matter.

## 6. GASDYNAMICS SIMULATIONS

### 6.1. Radial distribution of subhalos

In this section we consider the effects of gas cooling and starformation on the abundance and radial distribution of subhalos. Figure 5 compares the radial distribution of subhalos with  $M/M_{\text{vir}} > 10^{-4}$  and  $M/M_{\text{vir}} > 2 \times 10^{-3}$  in the  $N$ -body and gasdynamics simulations of the same cluster. These profiles are constructed by stacking five (nine) outputs between  $z = 0.25$  and  $z = 0$  for  $N$ -body (gasdynamics) simulation. The radial distribution of subhalos in the  $N$ -body and gasdynamics simulations are remarkably similar.<sup>4</sup> This indicates that the gas cooling has rel-

<sup>4</sup> Although we plot profiles normalized to  $\langle n_{\text{vir}} \rangle$  to compare to the DM profile, the values of  $\langle n_{\text{vir}} \rangle$  are the same in the gasdynamics and dissipationless run, as can be seen in Figure 1. The unnormalized profiles do match in the same way as in Figure 5.

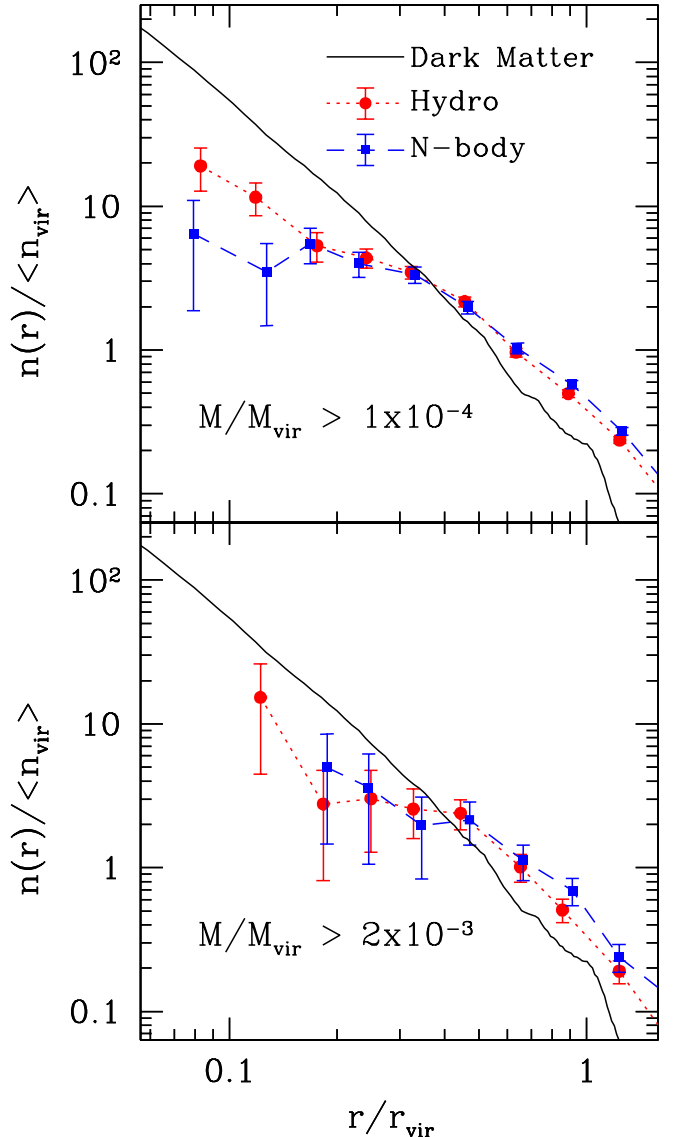


FIG. 5.— Radial profiles  $n(r)/\langle n_{\text{vir}} \rangle$  in gasdynamics (*dotted*) and  $N$ -body (*dashed*) runs for halos with  $M/M_{\text{vir}} > 10^{-4}$  (*top*) and  $M/M_{\text{vir}} > 2 \times 10^{-3}$  (*bottom*). The *solid line* shows the dark matter profile in the gasdynamics run. The radial distribution of subhalos is remarkably similar for these two runs, regardless of the mass cut. This indicates that gas cooling in our simulations does not significantly affect the survival of subhalos and their radial distribution.

atively little effect on the survival and radial distribution of subhalos. Although cooling can clearly help survival of subhalos in lower resolution simulations, the halos in our  $N$ -body simulations are apparently sufficiently dense to avoid premature disruption. Given the results of the recent studies of the causes of the overmerging problem (e.g., Moore et al. 1996; Klypin et al. 1999), this is not surprising. Gas cooling significantly affects mass distribution only in the inner few percent of the virial radius, while the survival is largely determined by the halo density within the radius of  $V_{\max}$  ( $\approx 2r_s$ ), just outside the affected regions. We should note that survival in the cluster core is probably enhanced by cooling. For the subhalos above the mass threshold of  $M/M_{\text{vir}} > 10^{-4}$ , the radial profile in



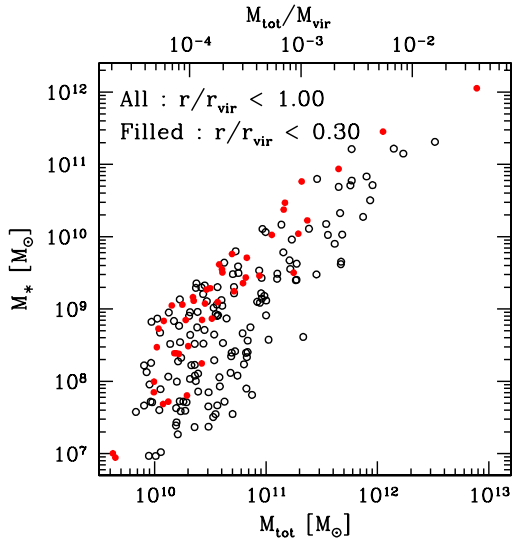


FIG. 6.— The mass of stars vs. the total mass of subhalos located within  $r_{\text{vir}}$  (all circles) and  $0.3r_{\text{vir}}$  (filled circles) of the host cluster. The plot shows that  $M_*$  scales with  $M_{\text{tot}}$  with large scatter, particularly for subhalos with  $M_{\text{tot}} < 10^{11} h^{-1} M_{\odot}$ . Note that the normalization of the relation changes in the inner regions of the cluster, probably due to the higher average tidal mass loss of the objects located there.

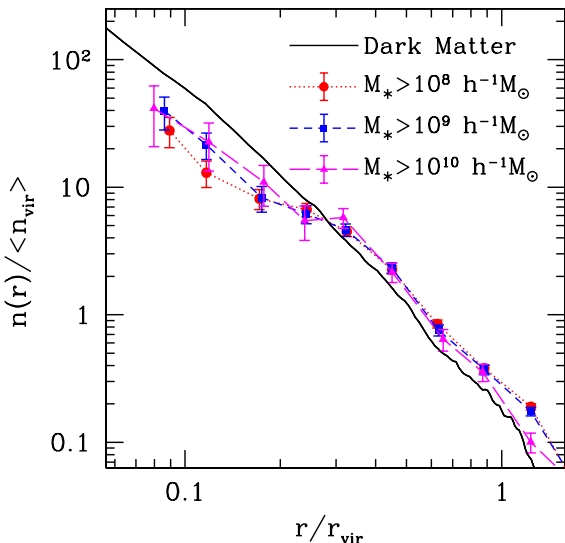


FIG. 7.— Radial profiles  $n(r)/\langle n_{\text{vir}} \rangle$  of subhalos selected using the stellar mass thresholds of  $M_* > 10^8$  (dotted),  $10^9$  (dashed) and  $10^{10} h^{-1} M_{\odot}$  (long-dashed) in the gasdynamics run. Note that the radial distribution of subhalos with the  $M_*$ -selection does not depend strongly on stellar mass threshold and is close to the radial density profile of dark matter.

the gasdynamics simulation is steeper than in the dissipationless run at  $r \lesssim 0.2r_{\text{vir}}$ . This, however, does not change the overall difference between subhalo and DM profiles at larger radii.

### 6.2. Radial distribution of galaxies

In reality, we observe galaxies, not subhalos, and it would be interesting to study the distribution of galaxies in simulations directly. To interpret the results, we first need

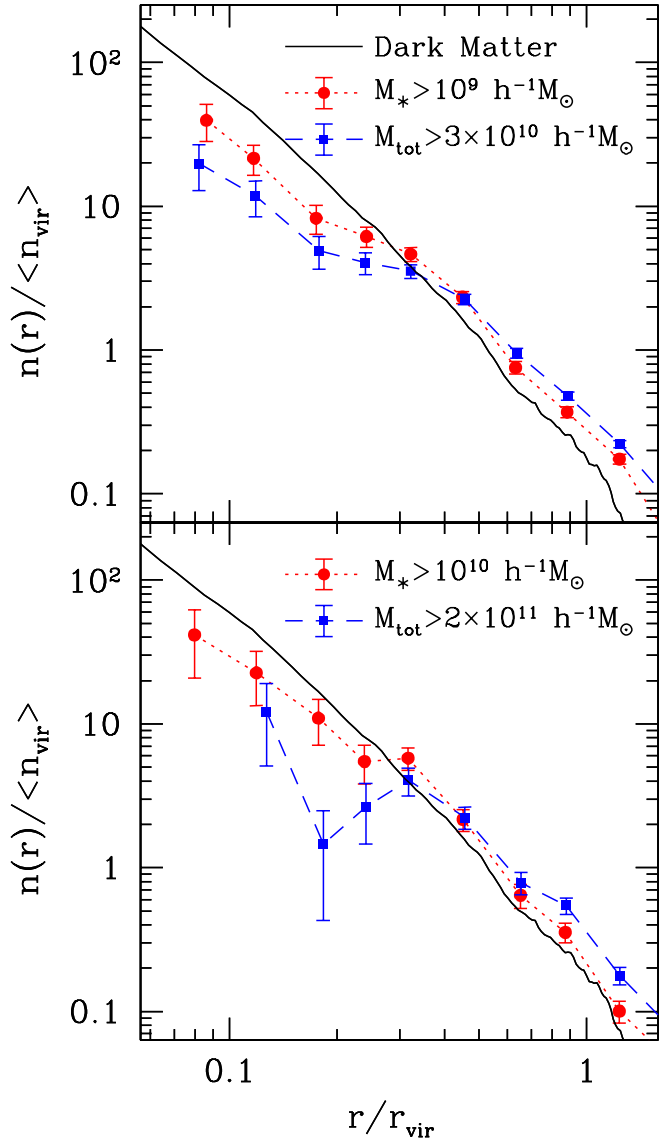


FIG. 8.— Radial profiles  $n(r)/\langle n_{\text{vir}} \rangle$  of subhalos in the gasdynamics run selected using the stellar mass (dotted) and corresponding total mass (dashed). The solid line shows the radial density profile of dark matter in the gasdynamics simulation. We show the profiles for two different mass thresholds:  $M_* > 10^9 h^{-1} M_{\odot}$  and  $M_{\text{tot}} > 3 \times 10^{10} h^{-1} M_{\odot}$  (top panel),  $M_* > 10^{10} h^{-1} M_{\odot}$  and  $M_{\text{tot}} > 2 \times 10^{11} h^{-1} M_{\odot}$  (bottom panel). Selection using stellar mass results in a significantly steeper radial profile.

to understand how stellar mass relates to the total mass of the host subhalo. We compute the stellar mass,  $M_*$ , as the mass enclosed within the tidal truncation radius of each subhalo. Figure 6 shows that the stellar mass of a galaxy,  $M_*$ , correlates with the subhalo mass,  $M_* \propto M_{\text{tot}}^{\alpha}$ . The slope of the correlation ranges in  $\alpha \sim 1 - 1.5$ . However, there is significant scatter, which becomes increasingly larger for the smaller subhalo masses. Note that the galaxies in the core of the cluster ( $r < 0.3r_{\text{vir}}$ ) populate the region of the plot near the upper envelope of points. In other words, for a given stellar mass, the total subhalo mass on average becomes smaller in the inner regions of cluster.

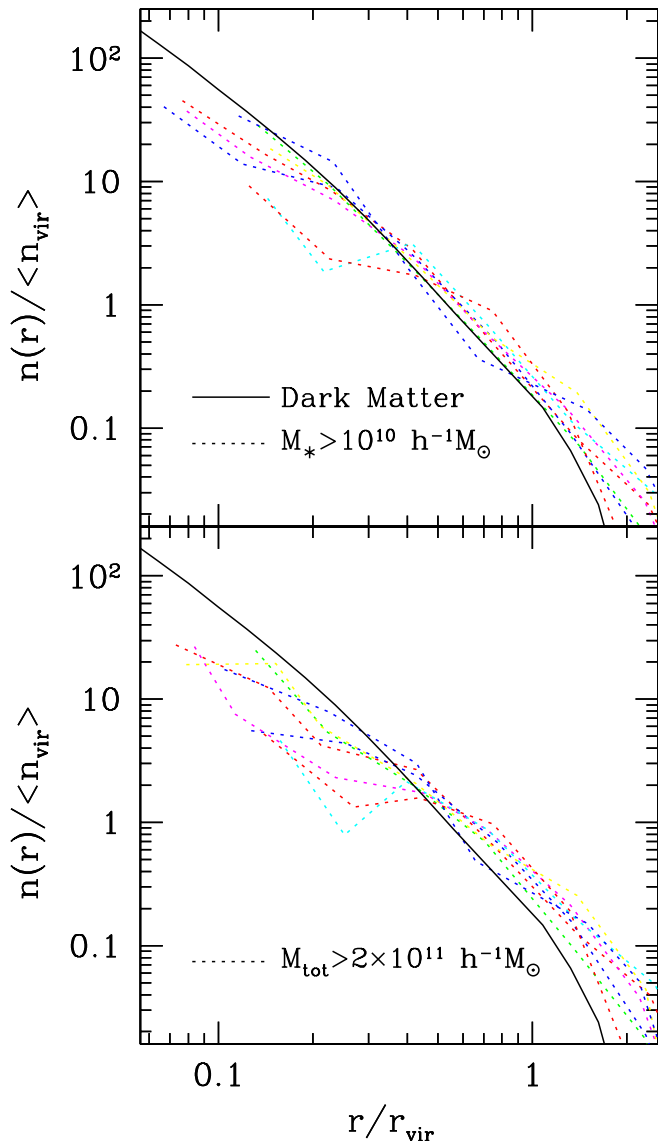


FIG. 9.— Radial profiles of subhalos  $n(r)/\langle n_{\text{vir}} \rangle$  for the eight simulated clusters at  $z = 0$ . Here, subhalos are selected using their stellar (*top*) and corresponding total (*bottom*) masses of  $M_* > 10^{10} h^{-1} M_\odot$  and  $M_{\text{tot}} > 2 \times 10^{11} h^{-1} M_\odot$  respectively. The solid line is the density profile of dark matter averaged over all clusters. The figure shows that the distribution of subhalos selected using  $M_*$  follows the dark matter profile at  $0.1 < r/r_{\text{vir}} < 1$  reasonably well. However, there is significant variation in the inner slope of the galaxy number density profiles among different clusters; for two out of the eight clusters the profile in the center is considerably shallower than that of the DM.

This systematic trend likely arises because the subhalos preferentially lose DM mass from their outer regions, while the tidal mass loss of more tightly bound stars is considerably smaller. In this case, as the subhalos are stripped and total mass decreases, the stellar mass stays approximately constant resulting in the evolution of points horizontally to the left in the  $M_{\text{tot}} - M_*$  plane. As we show in Figure 4, the subhalos in the cluster core on average have experienced larger tidal mass loss than the halos near the virial radius, which explains the systematic shift between solid and open points in Figure 6. The amount of tidal

mass loss experienced by each object depends on its epoch of accretion, orbital parameters, and to some extent on its internal structure. The evolutionary differences among subhalos would explain the large scatter of the  $M_{\text{tot}} - M_*$  correlation. The maximum circular velocity of subhalos in simulations with cooling changes much more slowly than the tidally bound total mass. Consequently, we find that the correlation of  $V_{\text{max}}$  and  $M_*$  is considerably tighter than the  $M_{\text{tot}} - M_*$  correlation (Nagai & Kravtsov 2004, in preparation).

Figure 7 shows the radial distribution of galaxies selected using three different stellar mass cuts:  $M_* > 10^8$ ,  $10^9$ , and  $10^{10} h^{-1} M_\odot$ . The figure shows that the radial distribution of galaxies with the stellar mass selection does not depend strongly on stellar mass and is close in shape to the dark matter profile at  $r \gtrsim 0.1 - 0.2 r_{\text{vir}}$ . Note that in the simulations with cooling, the DM profile at  $r \lesssim 0.1 r_{\text{vir}}$  is somewhat steeper than the corresponding profile in the dissipationless simulation (Gnedin et al. 2004). It is clear that  $M_*$ -based selection results in a radial distribution of galaxies which is considerably steeper than the radial profile of subhalo samples selected using total mass.

Figure 8 shows this more clearly using direct comparison of the radial distribution of objects selected using stellar and corresponding total mass. The thresholds in  $M_{\text{tot}}$  are chosen to correspond approximately to the  $M_*$  thresholds using the  $M_{\text{tot}} - M_*$  correlation (Figure 6). The figure shows that the radial distribution of objects in  $M_*$ -selected samples is significantly steeper than the profiles of objects selected by the total mass. As expected, the difference is similar to the difference of profiles of subhalos selected using total mass at  $z = 0$  and at the time of accretion, seen in § 5. The stars are located near the centers of DM subhalos and are tightly bound. The stellar mass thus should not evolve significantly even if an object sheds a large fraction of its DM halo (e.g., Gnedin 2003, and references therein). Our results show that this is indeed the case.

Since the results so far are based on the analyses of one cluster, we investigate if there is a variation in the distribution of galaxies among different clusters. Figure 9 shows the 3D radial distribution of galaxies for the sample of eight clusters at  $z = 0$ . We find that for all clusters the radial distribution of galaxies selected based on the stellar mass,  $M_*$ , is steeper than that of the samples selected using the total mass,  $M_{\text{tot}}$ . The figure also illustrates significant variation in the inner slope of the profile among different clusters. The radial profiles of galaxies in most clusters are close to the dark matter profiles at all radii, but there are some that show significant flattening of the galaxy number density profile at  $r \lesssim 0.3 r_{\text{vir}}$ . We find that the variation among profiles does not decrease if we use clusters at the epochs when they are most relaxed. This indicates that the flattening of the galaxy number density profile is not related to the host halo mass or to the dynamical state of clusters but may be related to their evolutionary histories.

It would also be interesting to ask whether the concentration of the radial profile of galaxies correlates with the concentration of the DM distribution. In Figure 10 we compare the concentration parameters of galaxies,  $c_{\text{Gal}}$ , and dark matter,  $c_{\text{DM}}$ , for the eight simulated clusters at



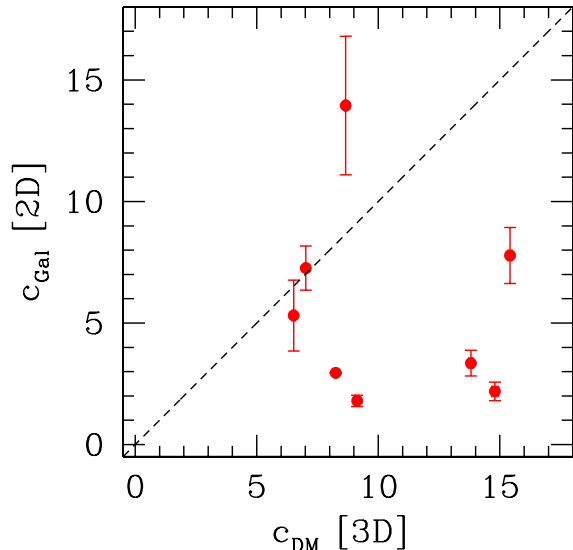


FIG. 10.— Comparison of the concentration parameters of galaxies,  $c_{\text{Gal}}$ , and dark matter,  $c_{\text{DM}}$ , for the eight simulated clusters at  $z = 0$ .  $c_{\text{Gal}}[2\text{D}]$ , is obtained by fitting the NFW profile to the projected (2D) galaxy distribution, whereas  $c_{\text{DM}}[3\text{D}]$ , is the concentration parameter of dark matter obtained by fitting the 3D dark matter profile.

$z = 0$ . For galaxies we use the concentrations obtained by fitting the projected Navarro-Frenk-White profile (hereafter NFW, Navarro et al. 1997) to the projected (2D) galaxy distribution, because the projected profiles are directly observable. For the dark matter, on the other hand, we use the true concentration obtained by fitting the NFW to the 3D dark matter distribution. The details of the fitting procedure are described in the Appendix.

The concentration parameters exhibit significant variation among different clusters. The concentration parameters of dark matter span a wide range from 6 to 16. Note that the concentration of dark matter in the current simulations may be systematically larger than the prediction of the dissipationless simulations (Navarro et al. 1997; Bullock et al. 2001; Eke et al. 2001; Tasitsiomi et al. 2004) because the baryon dissipation steepens the inner profiles of dark matter (Gnedin et al. 2004). Two of the eight clusters have very similar best fit concentrations of galaxy and DM profiles. There is also one cluster for which the concentration of galaxy profile is larger than that of dark matter. Nevertheless, the concentration parameter of galaxies in the majority of clusters is smaller than that of dark matter. These results indicate that fits to the projected radial profiles of galaxies may be a poor probe of the DM concentrations.

### 6.3. Comparison to observations

Here we compare the distribution of galaxies and subhalos in the  $\Lambda\text{CDM}$  clusters in our simulated sample to the observed galaxy distribution. Figure 11 shows the projected radial distribution of dark matter, galaxies and subhalos averaged over the eight simulated clusters at  $z = 0$ . The profiles are constructed by projecting spherical volume with radius of  $3r_{\text{vir}}$  centered on the cluster center

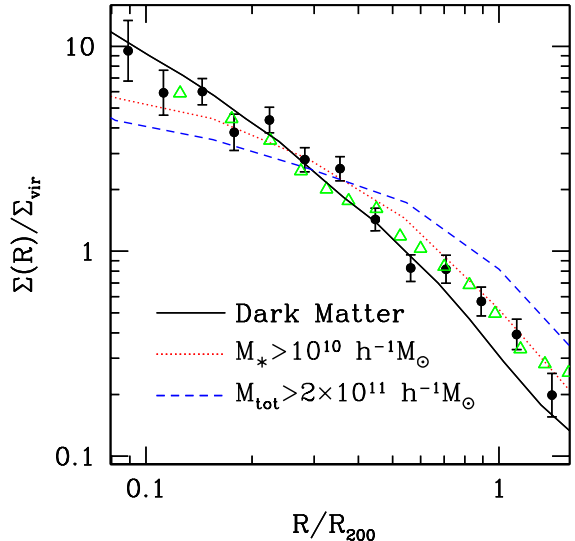


FIG. 11.— Projected radial distribution of galactic subhalos  $\Sigma(R)/\Sigma_{\text{vir}}$  averaged over the eight simulated clusters at  $z = 0$  and three orthogonal projections. We show the radial distribution of subhalos selected using the mass thresholds of  $M_* > 10^{10} h^{-1} M_{\odot}$  (dotted) and  $M_{\text{tot}} > 2 \times 10^{11} h^{-1} M_{\odot}$  (dashed). The solid line is the average projected profile of dark matter in the gasdynamics simulation. The *solid circles* are the average radial profile of galaxies in clusters in the CNOC survey (Carlberg et al. 1997), and the *open triangles* are the average profile in the 2MASS cluster survey (Lin et al. 2004). The data points are scaled arbitrarily. Note that the distribution of  $M_*$ -selected subhalos is consistent with the observed distribution of galaxies over the entire range of probed radii:  $0.1 < R/R_{200} < 2.0$ .

and averaging over all simulated clusters and three orthogonal projections of each cluster. The profiles are normalized in units of the mean surface density of dark matter,  $\Sigma_{\text{vir}} = M_{\text{vir}}/\pi r_{\text{vir}}^2$ , and galaxies/subhalos,  $N_{\text{vir}}/\pi r_{\text{vir}}^2$ , where  $M_{\text{vir}}$  and  $N_{\text{vir}}$  are the mass and the number of objects enclosed within the sphere with the virial radius  $r_{\text{vir}}$  respectively. The data points are from the CNOC (Carlberg et al. 1997) and 2MASS (Lin et al. 2004) cluster surveys. The observed galaxy profiles are scaled arbitrarily and the 2MASS survey profile has been re-binned to smaller number of bins for clarity.

The figure shows that the projected distribution of galaxies in both simulations and observations is more concentrated than that of subhalos selected using the total mass. The radial profile of galaxies is somewhat shallower than the average dark matter distribution. Nevertheless, the figure shows that the distribution of galaxies in the simulation is in reasonably good agreement with the observed distribution of galaxies for the entire probed range of scales:  $0.1 < R/R_{200} < 2.0$ . The agreement with the data is considerably better if two clusters with very flat inner profiles (see Figure 9) are excluded.

## 7. DISCUSSION AND CONCLUSIONS

We presented a study of the radial distribution of subhalos and galaxies using high-resolution cosmological simulations of galaxy clusters formed in the concordance  $\Lambda\text{CDM}$  cosmology. In this paper, we first analyze the dissipationless simulations to study properties and processes that govern the evolution of subhalos. We then analyze cluster

simulations with gasdynamics, cooling, and starformation started from the same initial conditions to study the effect of these processes on the spatial distribution of subhalos and galaxies.

In agreement with previous studies, we find that the radial profile of subhalos within the virial radius in the dissipationless simulations is significantly shallower than the dark matter distribution, if the subhalos are selected based on the present-day values of the subhalo mass,  $M^0$ . Comparing two simulations of the same cluster with an order of magnitude different resolution, we show that both the radial profile of subhalos and DM profiles have converged at the scales analyzed here. The difference between matter and subhalo distributions is therefore real and is not due to numerical overmerging, in agreement with conclusions of Diemand et al. (2004). Selection on the present-day value of the maximum circular velocity,  $V_m^0$ , results in steeper radial profile of subhalos. The radial bias with respect to the dark matter distribution in this case is weaker than in the case of mass-based selection.

We show that the radial bias of subhalo distribution is due to the tidal mass loss experienced by subhalos as they orbit in the cluster potential. We find that subhalos in the inner regions have on average suffered larger tidal mass loss than the halos near the virial radius (see also Gao et al. 2004b). For instance, the halos within  $0.3r_{\text{vir}}$  on average have lost more than 70% of their mass since accretion, while subhalos at  $r > 0.5r_{\text{vir}}$  on average lose only  $\lesssim 40\%$  of their mass. Mass-based selection, therefore, biases the subhalo sample to large radii where tidal stripping have depleted the number of objects in a given mass range to a lesser degree. The mass loss is also accompanied by decrease in the maximum circular velocity, but the decrease is slower compared to mass. The slower evolution of the maximum circular velocity compared to mass means that when it is used to select subhalos the radial bias is smaller.

One of the obvious omissions in dark matter only simulations is the lack of dissipation. One can thus ask whether the baryon dissipation makes the subhalo more resistant to tidal disruption. If so, is the effect strong enough to resolve the differences between matter and subhalo distribution? Comparing the simulations with and without cooling and starformation, we find that the baryon dissipation indeed increases the survival of subhalos, especially in the inner regions of clusters. However, the effect is relatively small because the baryon dissipation makes the core more resistant to the tidal disruption, but not the entire structure of the subhalo. The efficiency of tidal losses for the total mass is, therefore, largely unaffected by the baryon dissipation except in the center of the subhalos. Thus, we conclude that this effect alone does not resolve the differences between matter and subhalo distributions.

If the radial bias is due solely to the varying amount of mass loss at different radii, the bias can be minimized if we use a property of halos unaffected by the evolution. In dissipationless simulations such property can be computed at the actual time of accretion if the evolution of a halo is traced in time. For instance, the radial profiles of subhalos selected using mass or maximum circular velocity measured at the time of subhalo accretion onto cluster are very close to the cluster DM profile. The radial distribution of subhalos and inferences from comparisons

with observed radial distribution of galaxies in clusters therefore depend on the selection criteria used to define subhalo sample. Consequently, the differences between subhalo and galaxy radial distributions do not necessarily indicate that dissipationless simulations significantly underestimate the number of galactic halos in clusters (e.g., Diemand et al. 2004; Gao et al. 2004a). They may simply indicate a difference in selection criteria for subhalo and galaxy samples.

Unfortunately, halo properties at the time of accretion are not observable in reality. The stellar mass, however, is an observable that can behave similarly. Stellar mass of a galaxy should change little until it is almost fully destroyed by tides because stars are located in the centers of halos and are tightly bound. The total mass, on the hand, can decrease dramatically due to tidal stripping. Using the simulations that include cooling and starformation, we show that the radial distribution of subhalos selected based on the stellar mass is considerably steeper than the that of subhalos selected using the total masses in the same simulation.

We show that the profiles of galaxies in the simulations are in good agreement with the observed projected distribution of galaxies for the entire radial range probed by the current simulations:  $0.1 < R/R_{200} < 2.0$ . The NFW fits to the average profiles of eight simulated clusters at  $z = 0$  in the range  $0.1 < R/R_{200} < 1.0$  give the best-fit concentration parameter of  $c_{\text{Gal}} \approx 2 - 3$  for galaxies and  $c_{\text{DM}} \approx 10$  for the dark matter. In other words, the radial profile of galaxies selected using the stellar mass is, on average, somewhat more extended than the dark matter profile. Note that the values of  $c_{\text{Gal}}$  in our simulations are consistent with the observational estimates of  $c_{\text{Gal}} \sim 3 - 4$  (Carlberg et al. 1997; van der Marel et al. 2000; Lin et al. 2004). There are indications that in group-size systems galaxies have more extended radial profiles than DM (van den Bosch et al. 2004; Mathews et al. 2004). The concentration of DM profiles are expected to be in the range  $c_{\text{DM}} \sim 5 - 10$  (Navarro et al. 1997; Bullock et al. 2001; Eke et al. 2001; Tasitsiomi et al. 2004) or larger if the profiles are significantly affected by gas cooling (Gnedin et al. 2004). We do not find any strong correlation between galaxy and DM concentrations in simulated clusters (see Figure 10). Thus, our results imply that the projected radial profiles of galaxies in clusters may, in general, be a poor probe of the underlying dark matter distribution.

The fact that there is a difference between galaxy and DM radial profiles indicates that galaxies are affected by tides in the dense environment of the cluster cores. Higher-resolution simulations will be needed to test whether the amount of the stellar mass loss and efficiency of tidal disruption have converged. If the flattening of the inner profile of galaxies is due to real tidal mass loss or disruption experienced by galaxies, we expect to find a large amount of stellar debris in the cluster core. Therefore, the detailed studies of the properties and origin of the stellar debris and intracluster light should provide new insights into the connection between the evolution of galaxies in clusters and the formation of cD galaxies and their stellar envelopes.

We would like to thank Stefan Gottlöber for giving us the HR re-simulation of one of the clusters, and Argyro Ta-

sitsiomi for providing the NFW fitting code. AVK would like to thank Aspen Center for Physics and organizers of the “Starformation in galaxies” workshop for hospitality and productive atmosphere during completion of this paper. This project was supported by the National Science Foundation (NSF) under grants No. AST-0206216 and AST-0239759, by NASA through grant NAG5-13274, and by the Kavli Institute for Cosmological Physics at the University of Chicago. D.N. is supported by the NASA Graduate Student Researchers Program and by NASA LTSA grant NAG5-7986. The cosmological simulations used in this study were performed on the IBM RS/6000 SP4 system at the National Center for Supercomputing Applications (NCSA) and at the Leibniz Rechenzentrum Munich and the John von Neumann Institute for Computing Jülich.

## REFERENCES

- Avila-Reese, V., Firmani, C., Klypin, A., & Kravtsov, A. V. 1999, *MNRAS*, 310, 527
- Bartelmann, M. 1996, *A&A*, 313, 697
- Berlind, A. A., Weinberg, D. W., Benson, A. J., Baugh, C. M., Cole, S., Davé, R., Frenk, C. S., Jenkins, A., Katz, N., & Lacey, C. G. 2003, *ApJ*, 593
- Blanton, M., Cen, R., Ostriker, J. P., Strauss, M. A., & Tegmark, M. 2000, *ApJ*, 531, 1
- Bullock, J. S., Kolatt, T. S., Sigad, Y., Somerville, R. S., Kravtsov, A. V., Klypin, A. A., Primack, J. R., & Dekel, A. 2001, *MNRAS*, 321, 559
- Carlberg, R. G., Yee, H. K. C., & Ellingson, E. 1997, *ApJ*, 478, 462
- Colin, P., Klypin, A. A., & Kravtsov, A. V. 2000, *ApJ*, 539, 561
- Colin, P., Klypin, A. A., Kravtsov, A. V., & Khokhlov, A. M. 1999, *ApJ*, 523, 32
- Cooray, A. & Sheth, R. 2002, *Phys. Rep.*, 372, 1
- De Lucia, G., Kauffmann, G., Springel, V., White, S. D. M., Lanzoni, B., Stoehr, F., Tormen, G., & Yoshida, N. 2004, *MNRAS*, 348, 333
- Diemand, J., Moore, B., & Stadel, J. 2004, *MNRAS*, 352, 535
- Eke, V. R., Navarro, J. F., & Steinmetz, M. 2001, *ApJ*, 554, 114
- Ferland, G. J., Korista, K. T., Verner, D. A., Ferguson, J. W., Kingdon, J. B., & Verner, E. M. 1998, *PASP*, 110, 761
- Frenk, C. S., Evrard, A. E., White, S. D. M., & Summers, F. J. 1996, *ApJ*, 472, 460
- Frenk, C. S., White, S. D. M., Bode, P., Bond, J. R., Bryan, G. L., Cen, R., Couchman, H. M. P., Evrard, A. E., Gnedin, N., Jenkins, A., Khokhlov, A. M., Klypin, A., Navarro, J. F., Norman, M. L., Ostriker, J. P., Owen, J. M., Pearce, F. R., Pen, U.-L., Steinmetz, M., Thomas, P. A., Villumsen, J. V., Wadsley, J. W., Warren, M. S., Xu, G., & Yepes, G. 1999, *ApJ*, 525, 554
- Gao, L., De Lucia, G., White, S. D. M., & Jenkins, A. 2004a, *MNRAS*, 352, L1
- Gao, L., White, S. D. M., Jenkins, A., Stoehr, F., & Springel, V. 2004b, *MNRAS* submitted ([astro-ph/0404589](#))
- Ghigna, S., Moore, B., Governato, F., Lake, G., Quinn, T., & Stadel, J. 1998, *MNRAS*, 300, 146
- . 2000, *ApJ*, 544, 616
- Gnedin, O. Y. 2003, *ApJ*, 582, 141
- Gnedin, O. Y., Kravtsov, A. V., Klypin, A. A., & Nagai, D. 2004, *ApJ* submitted ([astro-ph/0406247](#))
- Goto, T., Yagi, M., Tanaka, M., & Okamura, S. 2004, *MNRAS*, 348, 515
- Guzik, J. & Seljak, U. 2001, *MNRAS*, 321, 439
- Katz, N., Hernquist, L., & Weinberg, D. H. 1992, *ApJ*, 399, L109
- Kennicutt, R. C. 1998, *ApJ*, 498, 541
- Klypin, A., Gottlöber, S., Kravtsov, A. V., & Khokhlov, A. M. 1999, *ApJ*, 516, 530
- Klypin, A., Kravtsov, A. V., Bullock, J. S., & Primack, J. R. 2001, *ApJ*, 554, 903
- Kravtsov, A. V. 1999, PhD thesis, New Mexico State University
- Kravtsov, A. V., Berlind, A. A., Wechsler, R. H., Klypin, A. A., Gottlöber, S., Allgood, B., & Primack, J. R. 2004a, *ApJ*, 609, 35
- Kravtsov, A. V., Gnedin, O. Y., & Klypin, A. A. 2004b, *ApJ*, 609, 482
- Kravtsov, A. V., Klypin, A., & Hoffman, Y. 2002, *ApJ*, 571, 563
- Lin, Y., Mohr, J. J., & Stanford, S. A. 2004, *ApJ*, 610, 745
- Mathews, W., Brighenti, F., & Boute, D. 2004, *ApJ* submitted
- Miller, C., Nichol, R., & et al. 2004, in preparation
- Mo, H. J. & White, S. D. M. 1996, *MNRAS*, 282, 347
- Moore, B., Katz, N., Lake, G., Dressler, A., & Oemler, A. 1996, *Nature*, 379, 613
- Navarro, J. F., Frenk, C. S., & White, S. D. M. 1997, *ApJ*, 490, 493
- Okamoto, T. & Habe, A. 1999, *ApJ*, 516, 591
- Okamoto, T. & Nagashima, M. 2001, *ApJ*, 547, 109
- Pearce, F. R., Jenkins, A., Frenk, C. S., Colberg, J. M., White, S. D. M., Thomas, P. A., Couchman, H. M. P., Peacock, J. A., Efstathiou, G., & The Virgo Consortium. 1999, *ApJ*, 521, L99
- Reed, D., Governato, F., Quinn, T., Gardner, J., Stadel, J., & Lake, G. 2004, *MNRAS* submitted ([astro-ph/0406034](#))
- Scherrer, R. J. & Weinberg, D. H. 1998, *ApJ*, 504, 607
- Seljak, U. 2000, *MNRAS*, 318, 203
- Springel, V., White, S. D. M., Tormen, G., & Kauffmann, G. 2001, *MNRAS*, 328, 726
- Taffoni, G., Mayer, L., Colpi, M., & Governato, F. 2003, *MNRAS*, 341, 434
- Tasitsiomi, A., Kravtsov, A. V., Gottlöber, S., & Klypin, A. A. 2004, *ApJ*, 607, 125
- Taylor, J. E., Silk, J., & Babul, A. 2003, in *IAU Symposium*, [astro-ph/0312086](#)
- Tormen, G., Diaferio, A., & Syer, D. 1998, *MNRAS*, 299, 728
- Tormen, G., Moscardini, L., & Yoshida, N. 2004, *MNRAS*, 350, 1397
- van den Bosch, F. C., Yang, X., Mo, H. J., & Norberg, P. 2004, *MNRAS* submitted, ([astro-ph/0406246](#))
- van der Marel, R. P., Magorrián, J., Carlberg, R. G., Yee, H. K. C., & Ellingson, E. 2000, *AJ*, 119, 2038
- Weinberg, D. H., Davé, R., Katz, N., & Hernquist, L. 2004, *ApJ*, 601, 1
- White, M., Hernquist, L., & Springel, V. 2001, *ApJ*, 550, L129
- White, S. D. M. & Rees, M. J. 1978, *MNRAS*, 183, 341
- Yoshikawa, K., Taruya, A., Jing, Y. P., & Suto, Y. 2001, *ApJ*, 558, 520

## APPENDIX

## NFW PROFILE FITTING PROCEDURE

For each halo, we fit the NFW analytic density profiles of the form

$$\rho(r) = \frac{\rho_s}{x(1+x)^2}, \quad (\text{A1})$$

$$\Sigma(r) = \frac{2\rho_s r_s}{x^2 - 1} f(x),$$

where with  $x \equiv r/r_s$ . The former is the 3D analytic NFW profile. The latter is the analytic 2D profile obtained by projecting the 3D profile along the line-of-sight from the negative to positive infinity, and  $f(x)$  is given by (Bartelmann 1996):

$$f(x) = \begin{cases} 1 - \frac{2}{\sqrt{x^2-1}} \arctan \sqrt{\frac{x-1}{x+1}} & (x > 1) \\ 1 - \frac{2}{\sqrt{1-x^2}} \operatorname{arctanh} \sqrt{\frac{1-x}{1+x}} & (x < 1) \\ 0 & (x = 1). \end{cases} \quad (\text{A2})$$

The NFW profile has two free parameters  $r_s$  and  $\rho_s$  or, equivalently, the concentration parameter  $c_{\text{vir}} \equiv r_{\text{vir}}/r_s$  and the virial radius  $r_{\text{vir}}$  of the halo. These parameters are highly degenerate, which makes the fits of the analytic profiles to the profiles of the simulated clusters sensitive to a number of factors, including the choice of binning, the merit function, the range of radii used in the fitting, the weights assigned to the data points. As we are only interested in the concentration parameters of galaxies and dark matter of the simulated clusters, we can improve the quality of the fits by removing the degeneracy between  $r_{\text{vir}}$  and  $c$ . This is possible because we can measure  $r_{\text{vir}}$  directly in the simulations, leaving concentration as the only one free parameter.

When fitting the profiles of the simulated clusters using the one-parameter NFW analytic profile, we first normalize the radius to the virial radius,  $y \equiv r/r_{\text{vir}}$ . For the

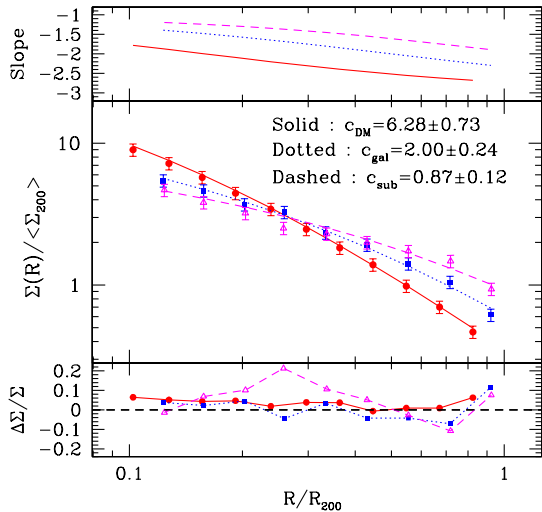


FIG. A12.— *Middle panel:* Results of the NFW fits to the projected radial distribution  $\Sigma(R)/\Sigma_{\text{vir}}$  of dark matter and galaxies averaged over the eight simulated clusters at  $z = 0$  and three orthogonal projections. The fits were done using the range  $[0.1r_{\text{vir}}, r_{\text{vir}}]$  and  $\chi^2$  merit function. Three lines indicate dark matter (*solid*) and galaxies selected using the thresholds of  $M_* > 10^{10} h^{-1} M_\odot$  (*dotted*) and  $M_{\text{tot}} > 2 \times 10^{11} h^{-1} M_\odot$  (*dashed*). *Bottom panel:* fractional deviations of each best fit NFW profile from the actual profile. *Top panel:* local logarithmic slope as a function of radius for the three fits. The distribution of both dark matter and galaxies is well-described by the NFW profile in the radial range  $0.1 < R/R_{200} < 1.0$ . We find that the radial distribution of galaxies is shallower than that of dark matter, with the concentration parameter of 6.3 for dark matter and concentration of 2.0 and 0.87 for subhalos selected using  $M_*$  and  $M_{\text{tot}}$ , respectively.

3D profile, we then need to normalize the analytic profiles in units of the mean mass density within the virial radius,  $\rho_{\text{vir}} = 3M_{\text{vir}}/4\pi r_{\text{vir}}^3$ . Similarly, for the projected (2D) profile, we normalize the profile in units of the projected surface mass density enclosed within the sphere with the virial radius,  $\Sigma_{\text{vir}} = M_{\text{vir}}/\pi r_{\text{vir}}^2$ . With this normalization, the NFW analytic density profiles in Eq. (A1) become

$$\begin{aligned} \frac{\rho(r)}{\rho_{\text{vir}}} &= \frac{1}{3} \frac{c^3 g(c)^{-1}}{cy(1+cy)^2}, \\ \frac{\Sigma(r)}{\Sigma_{\text{vir}}} &= \frac{1}{2} \frac{c^2 g(c)^{-1}}{(cy)^2 - 1} f(cy), \end{aligned} \quad (\text{A3})$$

with only one free parameter,  $c$ . Here,  $g(c) = \ln(1+c) - c/(1+c)$ .

For each halo, we obtain the best fit concentration parameter  $c$  by fitting the analytic profiles given by Eqs. (A3) to the 3D and 2D radial profiles of dark matter, galaxies and subhalos in the simulations by the standard  $\chi^2$  minimization. We use equal-size logarithmic bins and weigh each bin by the Poisson noise in the number of dark matter particles, galaxies or subhalos (see Tasitsiomi et al. 2004, for more details). For both dark matter and galaxies/subhalos, we perform fits using the 12 equal-size logarithmic bins between  $0.1 < r/r_{\text{vir}} < 1.0$ . The fitting region is chosen to maximize the statistics of galaxies, since the radial profiles of galaxies are much noisier than the dark matter profile. The lower radial bound is set by the fact that the halo finder fails to find galaxies within  $r/r_{\text{vir}} \lesssim 0.1$ , while the outer bound is the virial radius of

the cluster, beyond which the presence of strong fluctuations due to cluster substructure significantly biases fits of smooth analytic profiles. We checked that the results are not sensitive to the variation around the chosen number of bins and radial range. For example, decreasing the lower/upper bound by a factor of two change the resulting best fit concentration of dark matter by only about 10%. Note that the insensitivity of the results to the perturbation around the chosen fit parameters is partly because we removed the degeneracy between  $c$  and  $r_{\text{vir}}$  by measuring  $r_{\text{vir}}$  directly from the simulations. In fact, the same changes affect the results of the two-parameters fits much more dramatically. Figure A12 shows the best-fit concentration parameters of the dark matter and galaxy distribution averaged over eight simulated clusters at  $z = 0$ . We find that the concentration parameter is 6.3 for dark matter, 2.0 for galaxies (selected using  $M_*$ ) and 0.87 for subhalos (selected using  $M_{\text{tot}}$ ). Note that the average concentration parameter of DM obtained here is lower than the average value of  $\approx 10$  quoted in § 7. This is because fitting of the projected profiles generally biases the profile due to the projection from the large distances outside the virial radii, as we did not attempt to subtract the background in these two dimensional fits.